Journal of Energy Storage 141 (2026) 119110

Contents lists available at ScienceDirect

Journal of Energy Storage

journal homepage: www.elsevier.com/locate/est

Research Papers

Selenium-based hetero-circulene monolayer: Coexistence of gapped Dirac fermions, heavy fermions and semiconductivity in a single quantum platform with lithium-ion battery applications

Naga Venkateswara Rao Nulakani [a,b,*], Yarjan Abdul Samad [c], Ameen Shahid [d], Calvyn Howells [e], Dalaver Hussain Anjum [a,b,*]

[a] Department of Physics, Khalifa University of Science and Technology, Abu Dhabi, 127788, United Arab Emirates
[b] Center for the Catalysis and Separations, Khalifa University of Science and Technology, Abu Dhabi, 127788, United Arab Emirates
[c] Department of Aerospace Engineering, Khalifa University of Science and Technology, Abu Dhabi, 127788, United Arab Emirates
[d] Department of Chemical and Materials Engineering, New Uzbekistan University, Tashkent, Uzbekistan
[e] Environmental Health and Safety, College of Health Sciences, Abu Dhabi University, Abu Dhabi, 59911, United Arab Emirates

ARTICLE INFO

Keywords:
Two-dimensional materials Dirac materials
Massive fermions
Gapped Dirac fermions
Li-ion battery
DFT

ABSTRACT

Semiconductivity, Dirac fermions, and correlated heavy fermions typically emerge in distinct material classes, such as transition metal dichalcogenides, graphene, and magic-angle twisted bilayer graphene. Integrating all three quantum features into a single platform has long been a challenge. In this study, we introduce a two-dimensional selenium-based hetero-circulene (Se-HC) monolayer composed of a carbon–selenium framework and explore its properties using density functional theory. The Se-HC monolayer exhibits dynamical, thermal, and mechanical stability. Strikingly, its electronic structure reveals a rare coexistence of gapped Dirac fermions and heavy fermions, with linearly dispersive and flat bands near the Fermi level. The Dirac cones are isotropic, with a Fermi velocity of $\sim 1.94 \times 10^5$ m/s. A narrow direct band gap separates these states by 73 meV using PBE-GGA and 0.40 eV with HSE06, enabling semiconducting behaviour without sacrificing Dirac physics. The band gap is highly tuneable via mechanical strain, compressive strain increases it, while tensile strain reduces it. We also study quasi-one-dimensional derivatives, including nanoribbons and nanotubes, and assess potential of Se-HC as a lithium-ion battery anode. This integration of semiconducting, Dirac, and flat-band features positions Se-HC as a versatile platform for quantum materials, with promising implications for next-generation electronic and energy applications.

1. Introduction

Graphene, a remarkable two-dimensional (2D) material composed of carbon atoms arranged in a monolayer honeycomb lattice, has captivated scientists across physics, chemistry, and materials science due to its extraordinary properties and wide-ranging technological applications [1–5]. One of the most striking features of graphene is its unique electronic band structure, where the valence and conduction bands touch at K and K' points of the hexagonal Brillouin zone, giving rise to the so-called Dirac points [6,7]. In the vicinity of the Dirac points in momentum space, graphene exhibits a linear dispersion relation for both electron and hole energies. This linear dispersion results in quasiparticles that behave like massless Dirac fermions, setting graphene apart from conventional solid-state materials such as metals, semiconductors, and insulators. Unlike typical materials, where charge carriers possess an effective mass due to parabolic or nearly flat band dispersion, electrons and holes in graphene mimic relativistic particles, traveling at an exceptionally high Fermi velocity (v_f) of approximately 10^6 m/s [8]. This relativistic behaviour underlies several novel quantum phenomena exclusive to graphene. For instance, graphene supports Klein tunnelling [9,10], a counterintuitive effect where charge carriers can transmit through potential barriers with perfect transmission under certain conditions. It also exhibits ballistic transport over submicron distances, allowing electrons to move without scattering, which is highly desirable for high-speed electronic devices [11]. Additionally, the peculiar electronic structure of graphene also leads to the observation of a half-

* Corresponding authors at: Department of Physics, Khalifa University of Science and Technology, Abu Dhabi, 127788, United Arab Emirates.
E-mail addresses: naga.nulakani@ku.ac.ae (N.V.R. Nulakani), dalaver.anjum@ku.ac.ae (D.H. Anjum).

https://doi.org/10.1016/j.est.2025.119110
Received 10 July 2025; Received in revised form 1 October 2025; Accepted 20 October 2025
Available online 29 October 2025

integer quantum Hall effect, a signature of relativistic quantum mechanics in condensed matter systems [12]. Consequently, the study of 2D systems hosting Dirac bands remains a central research focus, inspiring the exploration of analogues such as graphynes [13–16], patterned graphenes [17], carbon nitrides [18], and metal borides [19,20], etc.

However, despite numerous extraordinary attributes of graphene, a key limitation lies in its lack of an intrinsic band gap [6,7]. For practical implementation in digital logic devices such as field-effect transistors (FETs), a material must reliably alternate between high-conducting and insulating states, necessitating a moderate-to-large band gap to achieve efficient switching [21]. The gapless nature of graphene results in low on/off current ratios, limiting its performance in transistor-based applications [22]. To overcome this, numerous methods have been proposed to engineer a band gap, including quantum confinement through nanostructuring into graphene nanoribbons (GNRs), nanotubes (GNTs), nanomeshes (GNMs), and quantum dots (GQDs), as well as via doping, chemical functionalization, or substrate-induced symmetry breaking [23,24]. While these approaches can introduce band gaps, they often achieve that at the cost of degrading carrier mobility or disrupting the linear dispersion relation critical to Dirac fermion behaviour. Furthermore, many of these techniques suffer from fabrication challenges such as non-uniform edge geometries, defect introduction, and scale-up limitations. As a result, a pressing challenge remains to discover or design a 2D material that intrinsically combines high mobility, tuneable electronic structure, and Dirac-like dispersion without reliance on structural compromises or external perturbations.

Extending beyond monolayer graphene, the vertical stacking of such 2D layers introduces an additional degree of structural and electronic tunability, culminating in the emergence of multilayered graphene systems [25,26]. Among these, bilayer graphene has attracted significant attention due to their distinct and tuneable electronic characteristics [27–30]. A critical factor governing these characteristics is the twist angle (θ) between the stacked layers. At large twist angles, the interlayer coupling becomes negligible due to significant momentum mismatch, effectively decoupling the two layers. This results in electronic properties resembling those of isolated monolayers. In contrast, at smaller twist angles, the layers interact more strongly due to enhanced interlayer tunnelling and hybridization [31]. Notably, bilayer graphene with AB stacking exhibits semi-metallic behaviour, characterized by quadratically dispersed bands and charge carriers with finite effective mass [25,30]. Even more intriguing is the behaviour of twisted bilayer graphene (TBG) at specific small twist angles, particularly around 1.1°, referred to as the 'magic angle' [32–34]. At this magic angle, the system exhibits a moiré superlattice that results in nearly flat electronic bands near the Fermi level. These flat bands correspond to a high density of states and dramatically suppressed Fermi velocity, amplifying the role of electron-electron interactions. Consequently, the system enters a strongly correlated regime, manifesting exotic quantum phases such as superconductivity [34], correlated insulating states [35], unusual magnetism [36], and a strange metallic state [37]. The discovery of magic-angle twisted bilayer graphene (MATBG) has ignited widespread interest in flat-band systems and their potential for hosting novel quantum phenomena [38–41].

At this juncture, the identification of a 2D material that intrinsically supports massless Dirac fermions, exhibits flat electronic bands, and possesses a tuneable semiconducting band gap would mark a transformative advance. Such a material would unify the desirable needs of high-speed transport and strong electron correlation, enabling access to exotic quantum phases such as superconductivity, magnetism, and charge ordering, all within a controllable electronic environment. This convergence of properties would surpass the limitations of gapless dispersion of graphene and circumvent the delicate lattice engineering required in moiré superlattices. Motivated by these ambitious goals, we have selected hetero[8]circulene (HC) as foundational molecular unit for constructing novel 2D monolayers [42]. These unique molecules are built upon a planar cyclooctatetraene core that incorporates both aromatic and antiaromatic subunits, imparting them with an unconventional hybrid electronic character. Recent investigations have revealed the structural and electronic properties of HC-based nanomaterials, highlighting their considerable promise across multiple application domains. For instance, Mineva and co-workers proposed tetraoxa[8]circulene-based nanosheets and nanotubes as promising nanophotonic materials, supported by first-principles calculations [43]. Yu et al. systematically explored the structural, mechanical, and electronic properties of various tetraoxa[8]circulene analogues, revealing strong visible-light absorption and a notably large Seebeck coefficient [44]. Kuklin et al. further demonstrated that fused tetraoxa[8]circulenes exhibit nontrivial topological features and high charge carrier mobilities, marking them as compelling candidates for next-generation quantum materials [45]. Beyond these studies, additional reports have proclaimed the potential of HC-based architectures in diverse applications, including sensing, molecular hosting, spin-based quantum information processing, and superconductivity [46,47]. Excitingly, in 2022, Coskun and co-workers successfully synthesized the first representative of HC-based nanomaterial, i.e., polymeric tetraoxa[8]circulene, and demonstrated the selective separation of Li^+ ions from complex mixtures containing Na^+, Ca^{2+}, and Mg^{2+} [48,49]. In another study, Li et al. reported significantly enhanced room-temperature gas-sensing capabilities for NO and NO_2 under the influence of an external electric field, revealing the field-tuneable sensitivity of these materials [50]. Additionally, Beskachko and colleagues investigated their hydrogen storage potential, suggesting that surface modification or metal-ion decoration may be essential to meet the requirements of practical hydrogen storage technologies [51]. Together, these findings elicit the broad functional potential of HC-based 2D systems for advanced applications in energy, sensing, and quantum materials research.

In this study, we investigate the selenium-based hetero-circulene (Se-HC) monolayer that seamlessly merges Dirac physics, flat-band characteristics, and semiconducting behaviour within a single, stable carbon-selenide lattice. Density Functional theory (DFT) calculations confirm its exceptional structural resilience and reveal an isotropic Dirac cone with direction-independent Fermi velocity and a narrow yet tuneable band gap, features rarely coexisting in a single material. This intrinsic electronic versatility, further enhanced by strain-induced modulation, positions the monolayer as a powerful candidate for next-generation quantum devices. Its extended potential, from quasi-one-dimensional architectures to high-efficiency lithium-ion storage, establishes it as a significant advancement in the design of multifunctional quantum materials.

2. Computational methods

First-principles calculations based on spin-polarized and non-spin-polarized density functional theory (DFT) were carried out using the Vienna Ab Initio Simulation Package (VASP) [52,53]. To ensure an accurate representation of core-valence electron interactions, we adopted the projector augmented wave (PAW) method, an advanced pseudopotential approach initially introduced by Blöchl [54]. This method effectively reduces computational costs while maintaining high precision in describing electronic structures. For the exchange-correlation functional, we selected the generalized gradient approximation (GGA) in the Perdew-Burke-Ernzerhof (PBE) parameterization, which is widely recognized for its reliability in predicting structural and electronic properties of materials [55]. A plane-wave basis set with a kinetic energy cutoff of 520 eV was applied to expand the electronic wavefunctions, ensuring a balance between computational efficiency and accuracy. The unit cell of the 2D monolayer was optimized using the Monkhorst-Pack k-point grid of $5 \times 5 \times 1$, while the electronic structure calculations were performed with a denser $11 \times 11 \times 1$ k-point grid to ensure convergence [56]. For the 1D nano analogues of the 2D monolayer, including nanoribbons (NRs) and nanotubes (NTs) extended along the x-

direction, geometry optimizations were carried out with a 5 × 1 × 1 k-point grid, and their electronic structures were computed using a denser 11 × 1 × 1 grid. These choices ensure accurate and well-converged electronic structure results for both 2D and 1D systems (see Supporting Information (SI), Fig. S1). The ab initio molecular dynamics (AIMD) simulations were performed using the canonical ensemble (NVT), in which the number of particles (N), volume (V), and temperature (T) are maintained constant. To minimize finite-size effects, a 2 × 2 × 1 supercell of the Se-HC monolayer was simulated. The AIMD simulations were performed for a total duration of 8 picoseconds (ps) with a time step of 1 femtosecond (fs). In these AIMD simulations, all forces as well as energies were computed directly from density functional theory (DFT) within VASP. Given the critical role of weak dispersion forces in adsorption and surface interactions, we incorporated van der Waals (vdW) corrections using the DFT-D3 method developed by Grimme et al. [57,58]. This approach explicitly accounts for long-range dispersion effects, improving the description of molecular and interfacial interactions. To prevent artificial periodic interactions, a vacuum spacing of 15 Å was introduced along the y- and z-directions, effectively isolating the 2D and 1D systems from its periodic images. This ensures that the calculated properties are free from spurious interactions due to the finite-size effects of the simulation cell.

3. Results and discussion

3.1. Structural details

Fig. 1a depicts the optimized 2D atomic structure of the 3 × 3 × 1 supercell of Se-based carbon hetero-circulene (Se-HC) monolayer. It clearly shows the connectivity between the adjacent Se-HC units and the nanoporous architectural features of Se-HC monolayer. The unit cell of the Se-HC monolayer is composed of a total of 24 atoms, which include both C and Se atoms as shown in Fig. 1b. The atomic composition exhibits a 5:1 carbon-to-selenium ratio, indicating a significant presence of carbon atoms in the material, which plays a crucial role in enhancing the structural stability. Within the unit cell, these atoms are arranged to form a highly ordered, planar network composed of interconnected carbon pentagons, octagons, and selenophene units. The carbon pentagons and selenophenes are attached to the rim of the carbon octagon, which sits at the center of the unit cell. This highly symmetric, square-like atomic arrangement belongs to tetragonal space group within the class of P4/mmm symmetry. The lattice vectors of 2D unit cell within this class are of equal length ($a = b = 9.295$ Å) and the angles between them are 90° ($\alpha = \beta = \gamma = 90°$). The C atoms in the Se-HC 2D monolayer are distributed across three distinct Wyckoff positions, labelled C1, C2, and C3, each corresponding to a unique crystallographic site (see Fig. 1b). The C1-type atoms are located at the 8*q* site with coordinates (0.31685, 0.57730, 0.50000) and are involved in the formation of the carbon octagon. The C2-type atoms occupy a different 8*q* site with coordinates (0.17338, 0.62401, 0.50000), where they are directly bonded to the C1 atoms, serving as connection points between C1, C3, and Se atoms. The C3-type atoms are located at the 4o site, with coordinates (0.07544, 0.50000, 0.50000), positioned at the periphery of the hetero-circulene unit and bonded to the C2 atoms, completing the carbon framework. In contrast, the Se atoms occupy a single inequivalent crystallographic position at the 4k site, with coordinates (0.17122, 0.17122, 0.50000), where they are bonded to the C2-type C atoms and located at the periphery of the hetero-circulene unit, similar to the C3-type C atoms. The Se-HC monolayer exhibits a range of bond lengths due to the diverse atomic constituents and their bonding environments. For example, the C1—C1 bond displays two distinct lengths of 1.39 Å and 1.44 Å, where the shorter bond (1.39 Å) is an integral part of the

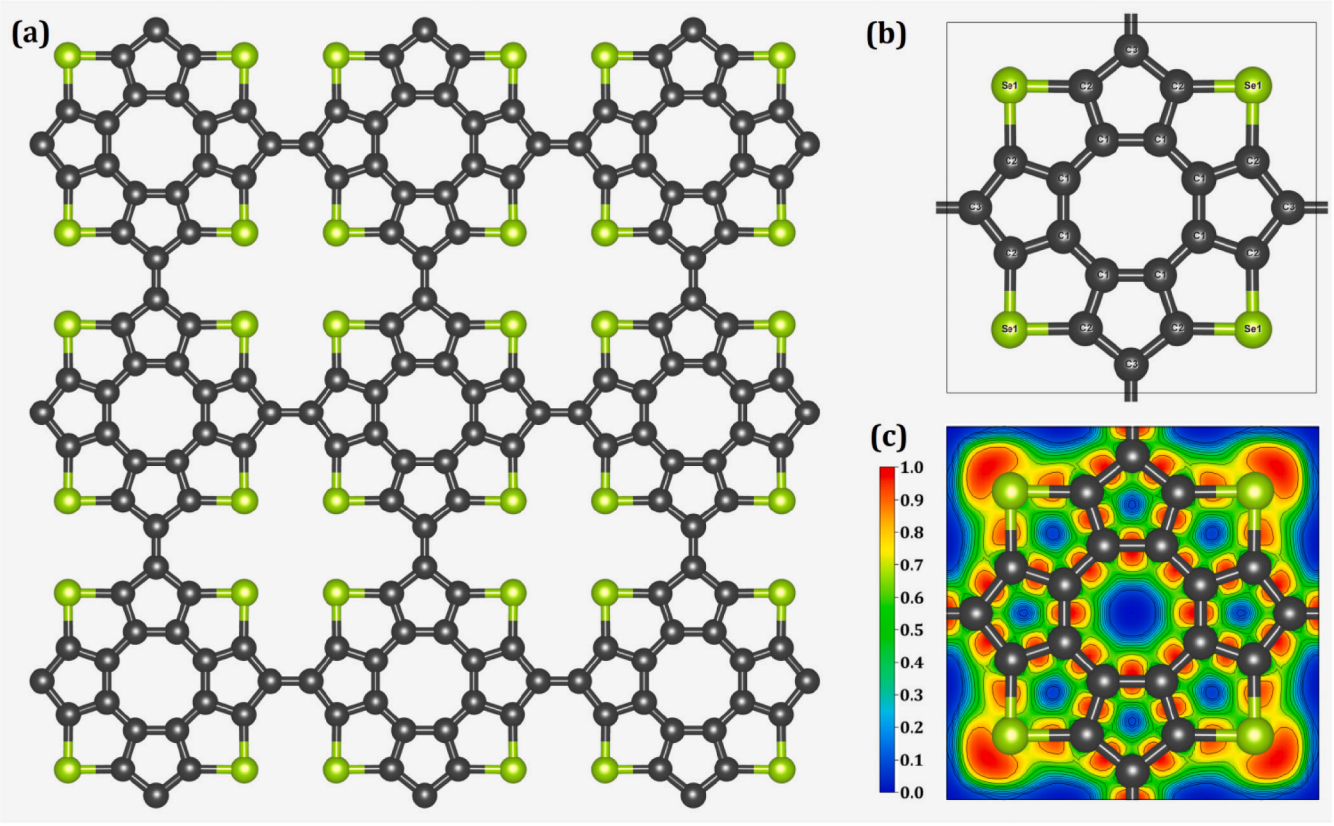

Fig. 1. (a) Optimized geometry of 3 × 3 × 1 super cell, (b) unit cell and chemically inequivalent carbon atoms, (c) electron localization function of Se-HC monolayer. Grey spheres are C atoms and green spheres are Se atoms. (For interpretation of the references to colour in this figure legend, the reader is referred to the web version of this article.)

selenophene unit, and the longer bond (1.44 Å) is an integral part of the carbon pentagon unit. The C1-type atoms are bonded to the C2-type C atoms with a bond length of 1.40 Å. The C2-type C atoms form bonds with the C3-type C and Se atoms, with bond lengths of 1.47 Å and 1.90 Å, respectively. Finally, the C3-type C atoms bond with other C3-type C atoms of the periodic unit cells, with a bond length of 1.40 Å. Overall, the bond lengths within the Se-HC monolayer range from 1.39 Å to 1.90 Å. Further bonding parameters are presented in Fig. S2. The electron localization function (ELF) of the Se-HC monolayer is presented in Fig. 1c. The colour scale ranges from 0 (deep blue), indicating strongly delocalized or electron-poor regions such as interstitial voids or vacuum spaces, to 1 (red), indicating fully localized electron density typically associated with covalent bonds or lone-pair regions. It clearly indicates the profound electron localization around the Se atoms, C—C and C—Se bonds, substantiating the presence of lone electrons, and covalent bonding.

We have further compared the areal density (ρ) and cohesive energy (E_c) of the Se-HC monolayer with a diverse set of pure-carbon and carbon selenide monolayers. For instance, the areal density of the Se-HC monolayer (0.28 atom/Å^2) is comparable to that of α-CSe (0.31 atom/Å^2) [59], β-CSe (0.25 atom/Å^2) [60] and h-CSe (0.28 atom/Å^2) [61]. However, the Se-HC monolayer exhibits a lower areal density than that of phagraphene (0.37 atom/Å^2) [17], graphene (0.38 atom/Å^2) [62], C_4Se (0.32 atom/Å^2), C_5Se (0.34 atom/Å^2) and C_6Se (0.32 atom/Å^2) [63]. This suggests the nano-porous nature of the Se-HC monolayer, potentially making it suitable for applications in energy storage and filtration (such as salts and water). The cohesive energy value (−6.69 eV/atom) of the Se-HC monolayer is significantly higher than those of previously reported carbon selenides, including α-CSe (−3.91 eV/atom) [59], β-CSe (−3.79 eV/atom) [60], h-CSe (−5.96 eV/atom) [61], C_4Se (−6.40 eV/atom), C_5Se (−6.43 eV/atom) and C_6Se (−6.54 eV/atom) [63]. Notably, the E_c of the Se-HC monolayer is also higher than that of some of the experimentally synthesized 2D materials, such as MoS_2 (−5.15 eV/atom) [64], phosphorene (−3.30 eV/atom) [64], highlighting the robust nature of the C—C and C—Se bonds inherent in the Se-HC monolayer. These results prove that the Se-HC monolayer is feasible to synthesize experimentally and characterized by its nano-porous structure.

3.2. Structural stabilities

To comprehensively assess the structural stability of the Se-HC monolayer, we performed an in-depth phonon band dispersion analysis combined with ab initio molecular dynamics (AIMD) simulations. These results, as shown in Fig. S3, provide compelling evidence for the dynamical stability of the Se-HC monolayer. Importantly, no unstable phonon modes were detected across the first Brillouin zone, confirming that the Se-HC monolayer remains free from vibrational instabilities. The absence of these unstable modes suggests that the Se-HC monolayer is resilient to small perturbations, such as thermal fluctuations or minor mechanical stresses. In addition to the phonon mode analysis, we extended our investigation to explore the thermal stability of the Se-HC monolayer using AIMD simulations. These simulations were conducted over a broad temperature range to examine the behaviour of the Se-HC monolayer under varying thermal conditions. The temperatures simulated included 300 K, 500 K, 1000 K, 1500 K, 2000 K, 3000 K, and 3500 K. Our AIMD results reveal that the Se-HC monolayer maintains its structural stability up to a maximum temperature of 3000 K. Throughout this wide temperature spectrum, no significant signs of degradation, phase transitions, or structural deformation were observed (see Figs. 2, S4, and S5). The remarkable ability of the Se-HC monolayer to withstand such high temperatures highlights its exceptional thermal stability, comparable to the renowned thermal resilience of graphene. These results underscore the potential of Se-HC monolayer for high-temperature applications, where traditional materials might degrade, including high-temperature electronics, nanomechanical devices, and other fields that demand reliable performance in harsh thermal conditions.

3.3. Mechanical properties

To comprehensively assess the mechanical properties and stability of the Se-HC monolayer, we systematically investigated its independent elastic stress tensors. Specifically, we analysed the elastic stress tensors C11, C12, and C66, which are essential in evaluating the mechanical stability of tetragonal two-dimensional materials. Our computed values of these elastic constants are C11 = 159.77 N/m, C12 = 24.66 N/m, and C66 = 25.31 N/m. The elastic stress tensor values satisfy the Born-Huang mechanical stability criteria, which are C11 > 0, C66 > 0, and C11 > |C12|. These results strongly suggest that the Se-HC monolayer exhibits robust mechanical stability, implying its resilience under mechanical stress. In addition to the elastic stress tensors, we explored the spatial dependence of the mechanical properties of the Se-HC monolayer by calculating the Young's modulus (Y) and Poisson's ratio (ν) across various directions within the unit cell. The results presented in Fig. 3a, reveal an anisotropic mechanical behaviour, where the Se-HC

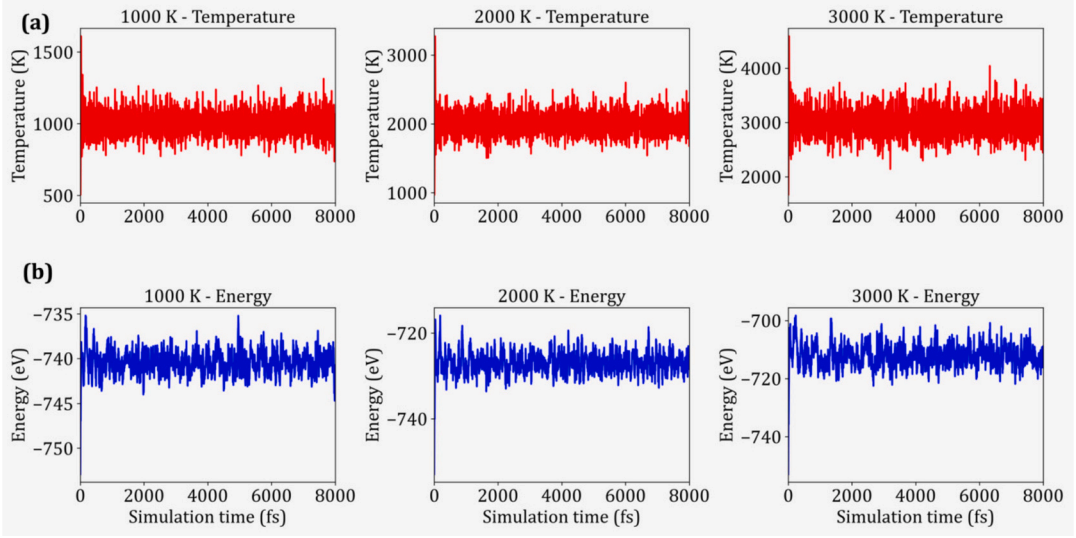

Fig. 2. Fluctuations of (a) temperature and (b) total energy during the AIMD simulations at 1000 K, 2000 K and 3000 K.

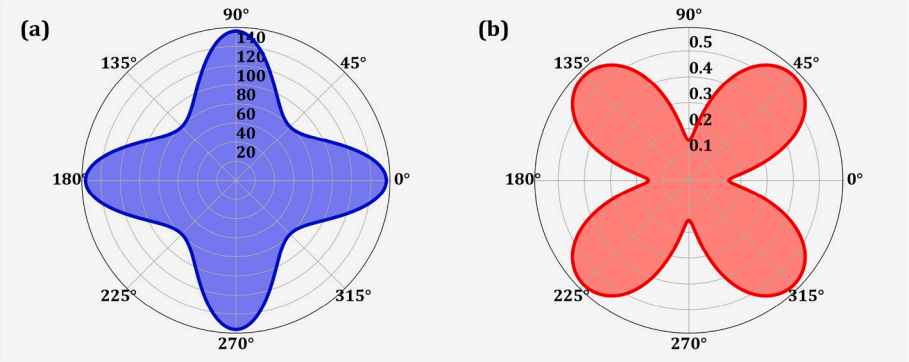

Fig. 3. Spatial dependent mechanical properties. (a) Young's modulus and (b) Poisson's ratio of Se-HC monolayer.

monolayer demonstrates maximum stiffness along the axial directions of the unit cell (at angles $\theta = 0°$, 90°, 180°, and 270°) with a Young's modulus of 156 N/m. This significant value along the axes indicates that the material is highly resistant to elastic deformation in these directions. Conversely, the Se-HC monolayer exhibits a minimum Young's modulus of 77 N/m along the diagonals of the unit cell (at $\theta = 45°$, 135°, 225°, and 315°), highlighting the relative flexibility of Se-HC monolayer along these directions. This anisotropy suggests that the Se-HC monolayer is more rigid along the principal axes and flexible along the off-axis directions, which is a crucial characteristic for applications requiring directional mechanical strength. We also analysed the directional variation of Poisson's ratio (ν) of Se-HC monolayer, which measures the lateral expansion or contraction of the monolayer when subjected to an axial strain. The results depicted in Fig. 3b, indicate that Poisson's ratio exhibits an inverse trend compared to Young's modulus, with a minimum value of 0.154 along the principal axes and a maximum value of 0.569 along the off-axis directions of the unit cell. The low Poisson's ratio ($\nu = 0.154$) along the axial directions implies that the monolayer has a high resistance to shape deformation and minimal lateral expansion under tensile stress. In contrast, the high Poisson's ratio ($\nu = 0.569$) along the diagonals suggests that the material undergoes significant lateral expansion when stretched in these directions, which is a characteristic behaviour of materials with high ductility.

3.4. Electronic properties

3.4.1. Electronic properties of pristine Se-HC monolayer

To gain profound insight into the conducting properties of the Se-HC monolayer, we conducted a comprehensive analysis of the electronic band structure. This investigation is pivotal for understanding the electronic fingerprint of the material, such as the nature of charge carriers, band gap characteristics, and fermion mobility. Moreover, by unraveling the electronic properties of the Se-HC monolayer, we can effectively assess its potential for various applications, particularly in advanced electronic and optoelectronic devices. To this end, the electronic structure of the Se-HC monolayer has been computed along the high-symmetry points within the irreducible Brillouin zone of the first tetragonal Brillouin zone, specifically along the path Γ (0.0, 0.0, 0.0) → X (0.5, 0.0, 0.0) → M (0.5, 0.5, 0.0) → Γ(0.0, 0.0, 0.0), as illustrated in Fig. 4a. This path is strategically chosen as it leverages the symmetry of the crystal lattice, thereby eliminating the need to probe the entire Brillouin zone while still achieving a comprehensive understanding of the electronic behaviour of the Se-HC monolayer. Fig. 4b reveals that two valence bands (VBs) near the Fermi level exhibit degeneracy at the corner high symmetry special point M of the Brillouin zone. For clarity, the valence bands are labelled as VB1 and VB2, descending from the Fermi level, i.e., VB1 lies directly below the Fermi level, while VB2 follows beneath it. Similarly, the conduction bands are denoted as CB1 and CB2, with CB1 being the band closest to the Fermi level. The remarkable feature of the electronic structure of Se-HC monolayer is that

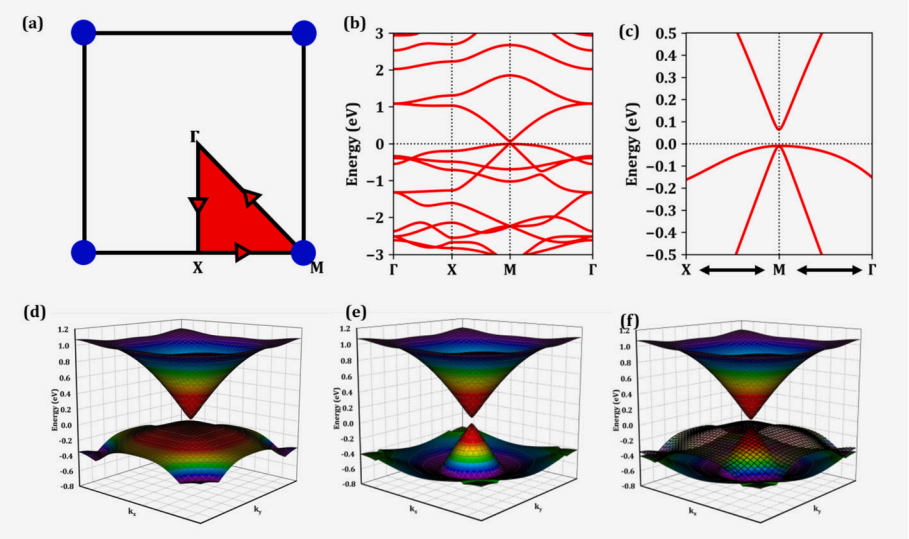

Fig. 4. (a) Tetragonal and irreducible Brillouin zone of Se-HC monolayer. (b) Electronic structure of Se-HC monolayer. (c) Amplified electronic structure around the high-symmetry special point, M. 3D band structure of (d) VB1 and CB1, (e) VB2 and CB1 and (f) VB2, VB1 (black mesh) and CB1.

the VB1 is nearly dispersionless along the high-symmetry special path X → M → Γ. This flat band characteristic indicates a high density of states and suggests the possibility of localized electronic states. In contrast, VB2 and CB1 exhibit a linear dispersion relation along the same high-symmetry path as shown in Fig. 4c. The linearity is indicative of massless Dirac fermion behaviour, which is often associated with high charge carrier mobility and enhanced conductivity. To gain deeper insights into the nearly dispersion-less and the linearly dispersed band characteristics of the Se-HC monolayer, we computed the 3D energy dispersion of the VB1, VB2 and CB1. As illustrated in Fig. 4d–f, VB2 and CB1 exhibit cone-like features in momentum space near the Fermi level. These energy cones closely resemble the Dirac cones observed in graphene, however, they are separated by a narrow direct bandgap, earning them the designation of gapped Dirac cones. This nonzero electronic gap results in a small but finite effective mass for the charge carriers, which deviates from the behaviour of truly massless Dirac fermions. Hence, we referred these charge carriers as gapped Dirac fermions similar to the previous studies [65–69]. A striking feature of these Dirac cones is their high degree of isotropy, as they display an identical slope along all crystallographic directions. This isotropy implies that the charge carriers in the Se-HC monolayer, both electrons (CB1) and holes (VB2), experience uniform velocity regardless of the direction of motion within the material. To further quantify this behaviour, we computed the radial Fermi velocities of the electrons and holes using the Fermi velocity equation:

$$v_f = \frac{1}{\hbar}\frac{\partial E}{\partial k}$$

where v_f is the Fermi velocity, E is the energy of the band, k is the wave vector, and $\hbar$ is the reduced Planck's constant. The results reveal that fermions residing within these cone-shaped bands move with an isotropic Fermi velocity of approximately 1.94×10^5 m/s. This value is comparable to the Fermi velocity observed in broad range of 2D Dirac materials, further highlighting the potential of the Se-HC monolayer for high-speed electronic applications. On the other hand, the holes in the VB1 are relatively massive (1.11–2.23 m_0) and exhibit lower mobilities. Unlike graphene and other 2D Dirac materials, the Se-HC monolayer exhibits a narrow direct bandgap of 73 meV at the M point. However, it is well-established that the PBE-GGA underestimates the bandgap of semiconductors. To achieve a more accurate bandgap estimation, the Heyd-Scuseria-Ernzerhof hybrid functional (HSE06) was employed. This method incorporates a portion of exact exchange from Hartree-Fock theory and exchange-correlation terms from traditional density functional theory (DFT) functionals, as parameterized in 2006. By utilizing the HSE06 functional, the bandgap of the Se-HC monolayer increases to 0.4 eV, making it more suitable for semiconducting applications. Generally, incorporating spin-orbit coupling has a profound effect on the electronic properties of the materials composed of heavy elements. However, we noticed that the spin-orbit coupling has a negligible effect on the electronic band profiles or energy gap of the Se-HC monolayer (see Fig. S6).

As shown in Fig. 5a, the total density of states (TDOS) and the atom- and orbital-projected density of states (PDOS) of the Se-HC monolayer were analysed to investigate the atomic orbitals contributing to the distinct Dirac electronic features near the Fermi level. The focus was on understanding the nearly dispersion-less VB1, along with the linearly dispersive VB2 and CB1 bands. The analysis reveals that the bonding and antibonding states of the π orbitals, primarily associated with the C and Se atoms, are key to the formation of these electronic bands. We performed a detailed orbital band decomposition analysis of the CB1, VB1 and VB2 to further substantiate these findings. This decomposition reinforces the critical involvement of the π and π* orbitals in the formation and dispersion characteristics of the bands near the Fermi level (see Fig. 5b). These findings are fully consistent with the orbital-projected electronic structures, shown in Fig. S7. Overall, the combination of these unique band features, including the flat VB1 and the linear dispersion of VB2 and CB1, highlights the potential of the Se-HC monolayer for applications in nanoelectronics, where both high mobility and strong electronic interactions are desirable.

3.4.2. *Influence of strain on electronic structure of Se-HC monolayer*

The application of external strain plays a crucial role in tuning the electronic properties of 2D materials, including the Se-HC monolayer. To systematically investigate this effect, we applied a bi-axial strain (σ) ranging from −0.05 (compressive strain) to +0.05 (tensile strain) in increments of 0.01. This approach allows us to understand how structural modifications influence the band structure and electronic behaviour of the Se-HC monolayer. The applied strain is calculated using the following expression,

$$\sigma = \frac{l - l_0}{l_0}$$

where, l_0 represents the equilibrium lattice constant, while l denotes the lattice constant under the applied strain. A negative value of σ corresponds to compressive strain, which reduces the lattice constant, whereas a positive value indicates tensile strain, leading to an expansion of the lattice. Our computational analysis reveals a remarkable strain-dependent modulation of the electronic properties of the Se-HC monolayer as depicted in Fig. 6. Specifically, the narrow direct bandgap exhibits a distinct response to both compressive and tensile strains. Within the compressive strain regime, the bandgap increases monotonically, reaching a maximum value of 0.27 eV at σ = −0.05. Conversely, as the tensile strain increases, the bandgap decreases and eventually closes at σ = 0.03, transforming the Se-HC monolayer into a zero-bandgap semimetal. Notably, in the tensile strain range of 0.04 to 0.05, the initially degenerate VB1 and VB2 states become non-degenerate as VB2 shifts to lower energy levels with increasing strain. Further, the nondispersive nature of VB1 becomes more pronounced with the tensile strain, leading to a more strongly correlated electronic regime. To further assess potential topological features, we computed the Z_2 index across the full strain window. In all cases, the Z_2 index remained zero, confirming that the system preserves a trivial electronic phase. Hence, although tensile strain significantly modifies the electronic landscape of the Se-HC monolayer, it does not induce a transition into a topologically nontrivial phase.

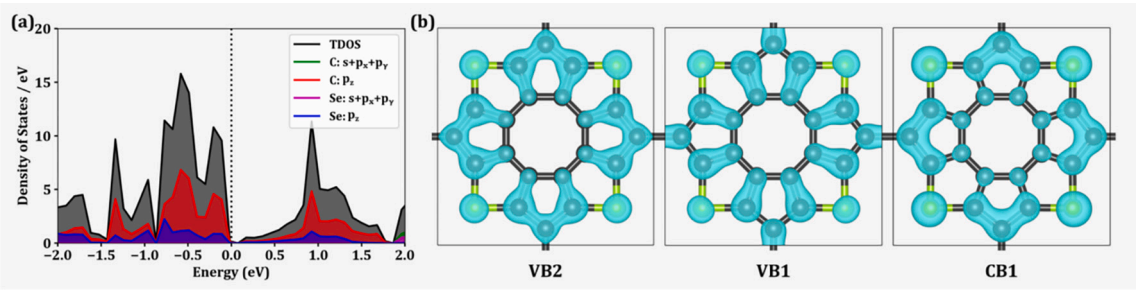

Fig. 5. (a) Total and partial density of states and (b) decomposed charge densities corresponding to the VB2, VB1 and CB1.

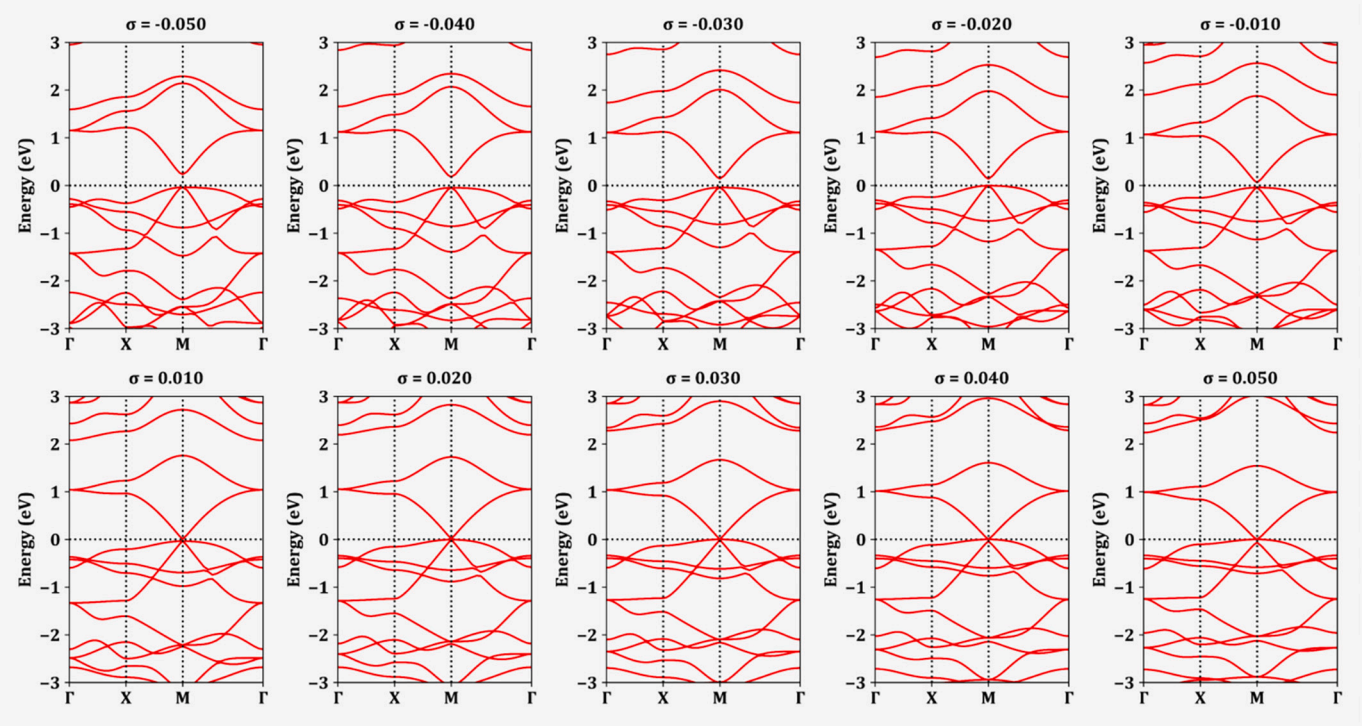

Fig. 6. Influence of bi-axial compressive and tensile strain on the electronic structure of Se-HC monolayer.

3.5. Optical properties

To unveil the applicability of the Se-HC monolayer in optoelectronic applications, we have computed the significant optoelectronic parameter, such as the imaginary part ($\varepsilon_2(\omega)$) of the complex dielectric function. As shown in Fig. 7, $\varepsilon_2(\omega)$ for the pristine system ($\sigma = 0$) displays two prominent absorption peaks at approximately 0.5 eV (p1) and 1.2 eV (p2), corresponding to strong interband transitions. The first peak lies in the near infrared region and likely originates from low-energy electronic transitions, while the second peak falls within the visible range, indicating the material is suitable for absorbing visible light. When compressive strain ($\sigma = -0.05$) is applied, both peaks shift slightly to higher photon energies, with a slight change in intensity. This behaviour suggests that strain affects the electronic band structure, mainly by altering transition energies while keeping the overall absorption strength similar. This tunability confirms that the Se-HC monolayer is a promising material for flexible optoelectronic devices such as infrared photodetectors and solar energy harvesters.

3.6. Electronic properties of one-dimensional Se-HC nanomaterials

The one-dimensional (1D) counterparts of 2D materials, such as nanoribbons (NRs) and nanotubes (NTs), have garnered significant attention due to their ability to inherit and often enhance the exceptional electronic properties of their parent 2D materials. These 1D nanoanalogues offer unique quantum confinement effects and edge states, which further modify the electronic behaviour, making them highly desirable for next-generation nanoelectronics applications. In this section, we embark on an in-depth exploration of the electronic characteristics of Se-HC NRs and NTs, derived from the pristine Se-HC monolayer. Our objective is to unravel how the quantum confinement and curvature effects influence the electronic specifics of these 1D structures. We systematically constructed Se-HC nanoribbons of varying widths (N), ranging from $N = 1$ to $N = 6$, as depicted in Fig. 8a. The unsaturated carbon atoms at the edges were passivated with hydrogen atoms to maintain electroneutrality and suppress edge states that could artificially distort the electronic properties. All the Se-HC NRs exhibit an electronic structure similar to that of 6 Se-HC NR, as shown in Fig. 9a.

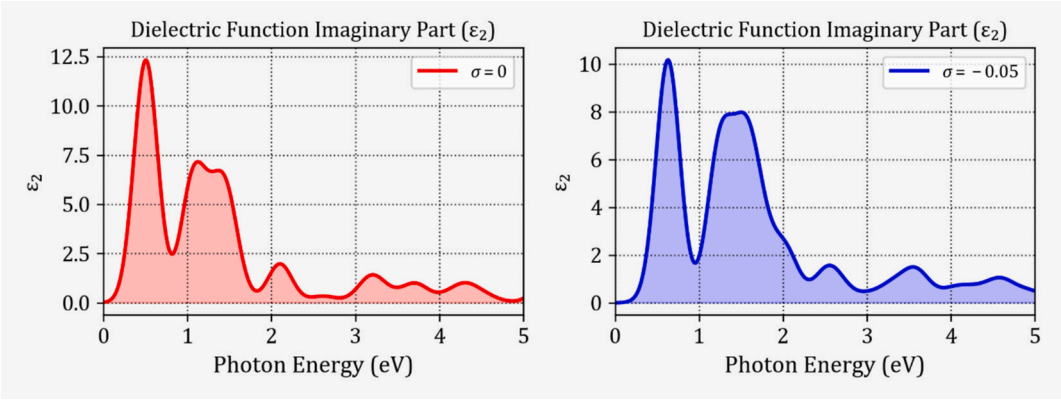

Fig. 7. Imaginary part ($\varepsilon_2(\omega)$) of the complex dielectric function of pristine ($\sigma = 0$) and strained ($\sigma = -0.05$) Se-HC monolayer.

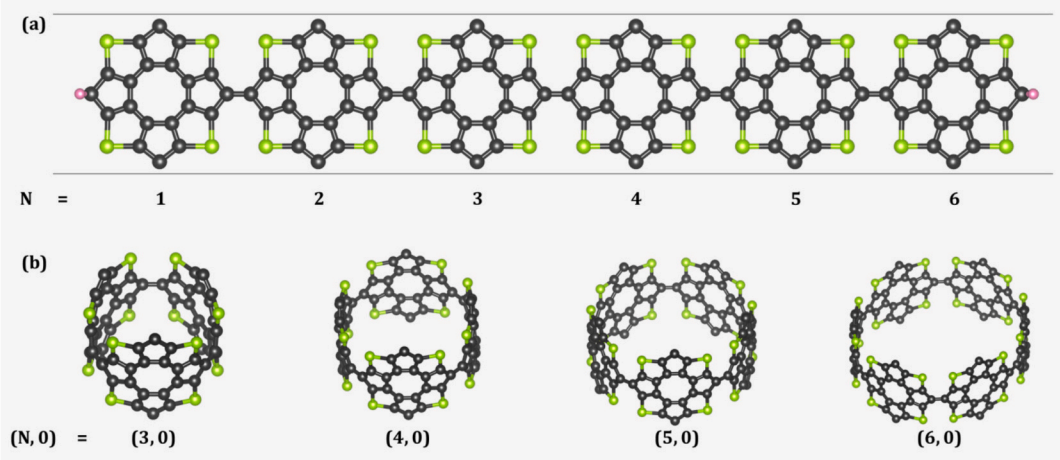

Fig. 8. Quasi-one-dimensional derivatives of Se-HC monolayer. (a) Se-HC nanoribbons (Se-HC NRs) with different widths (N) and nanotubes (Se-HC NTs) with different chirality.

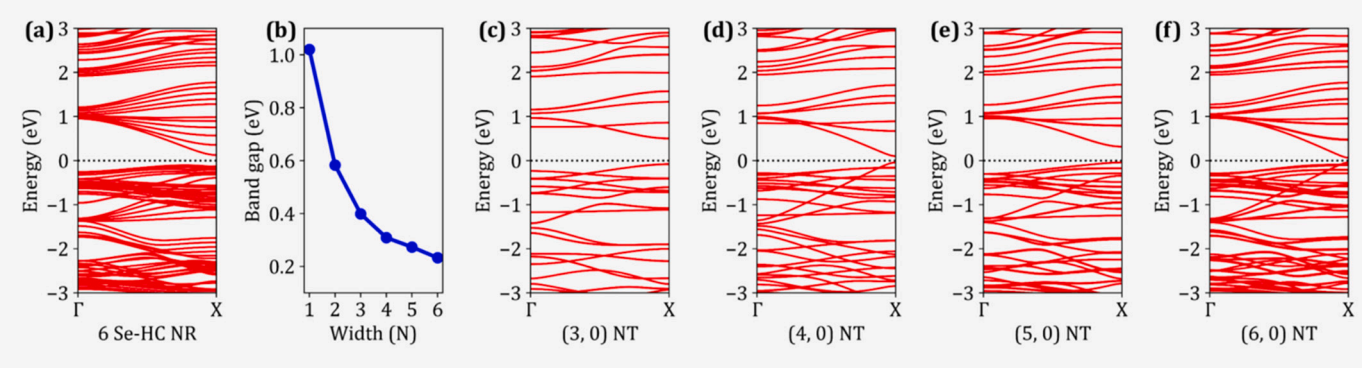

Fig. 9. Electronic structure of quasi-one-dimensional derivatives of Se-HC monolayer. (a) 6 Se-HC nanoribbon, (b) variation of band gap with respect to width (N) of Se-HC NRs. Band structure of (c) (3, 0) (d) (4, 0) (e) (5, 0) and (f) (6, 0) Se-HC nanotubes.

Our DFT analysis reveals a decreasing band gap trend with increasing NR width (see Fig. 9b). Specifically, the narrowest nanoribbon (1-Se-HC NR) exhibits a band gap of 1.02 eV, while the widest nanoribbon (6-Se-HC NR) shows a significantly reduced band gap of 0.23 eV. This gradual band gap reduction is attributed to the quantum confinement effect, where the increased ribbon width leads to enhanced delocalization of electronic states, effectively narrowing the band gap. Similarly, to further explore the curvature-induced effects on electronic behaviour, we rolled the Se-HC nanoribbons into Se-HC nanotubes with varying diameters. The nanotubes were constructed from 3, 4, 5, and 6 Se-HC NRs, and labelled as (3,0), (4, 0), (5, 0), and (6, 0) NTs, respectively, as illustrated in Fig. 8b. Our results indicate that all the NTs exhibit semiconducting behaviour with a narrow direct band gap, which is highly sensitive to the nanotube diameter and curvature. Notably, the even-indexed (N,0) NTs exhibit a comparatively lower band gap than their odd-indexed counterparts, highlighting the chirality-dependent electronic behaviour in Se-HC nanotubes as depicted in Fig. 9c–f. In essence, the band gap tunability achieved through controlling the nanoribbon width and nanotube curvature underscores the potential of Se-HC-based 1D nanostructures for next-generation nanoelectronic and optoelectronic devices. The ability to manipulate the electronic band structure through geometric modification offers exciting prospects for designing flexible, high-performance semiconducting materials for quantum transport and energy applications.

4. Anode performance for Li-ion batteries

In this section, we present the potential of the Se-HC monolayer for Li-ion battery anode material applications [70]. We have estimated this performance by evaluating following important parameters pertaining to the Li-ion battery anode material, which include (a) binding energy of Li atoms (E_{ads}), (b) diffusion energy barriers (E_a), (c) open circuit voltage (OCV), (d) theoretical storage capacity (TSC).

The Se-HC monolayer features five different binding sites, namely (i) the central position of the four Se atoms (P1), (ii) the central position of the carbon pentagon (P2), (iii) the central position of the selenophene unit (P3), (iv) the central position of four C and two Se atoms (P4), and (v) the central position of the octagon unit (P5) as shown in Fig. 10a. The adsorption energies (E_{ads}) at each binding site are calculated using the following formula,

$$E_{ads} = \frac{E_{Li@Se-HC} - (E_{Se-HC} + nE_{Li})}{n}$$

where E_{Se-HC} and $E_{Li@Se-HC}$ specifies the energies of the Se-HC monolayer before and after the adsorption of the Li atom. The bulk Li metal energy per atom is used to substitute the E_{Li} and n is the total number of Li atoms involved in the adsorption process. Our results indicate that lithium atoms preferentially adsorb at specific sites, with the most stable binding occurring at the P1 site (−0.65 eV), followed by P2 (−0.64 eV), P3 (−0.59 eV), P4 (−0.57 eV), and P5 (−0.47 eV). To gain deeper insights into the nature of the adsorption process, we conducted Bader charge analysis, which revealed a significant charge transfer from the lithium

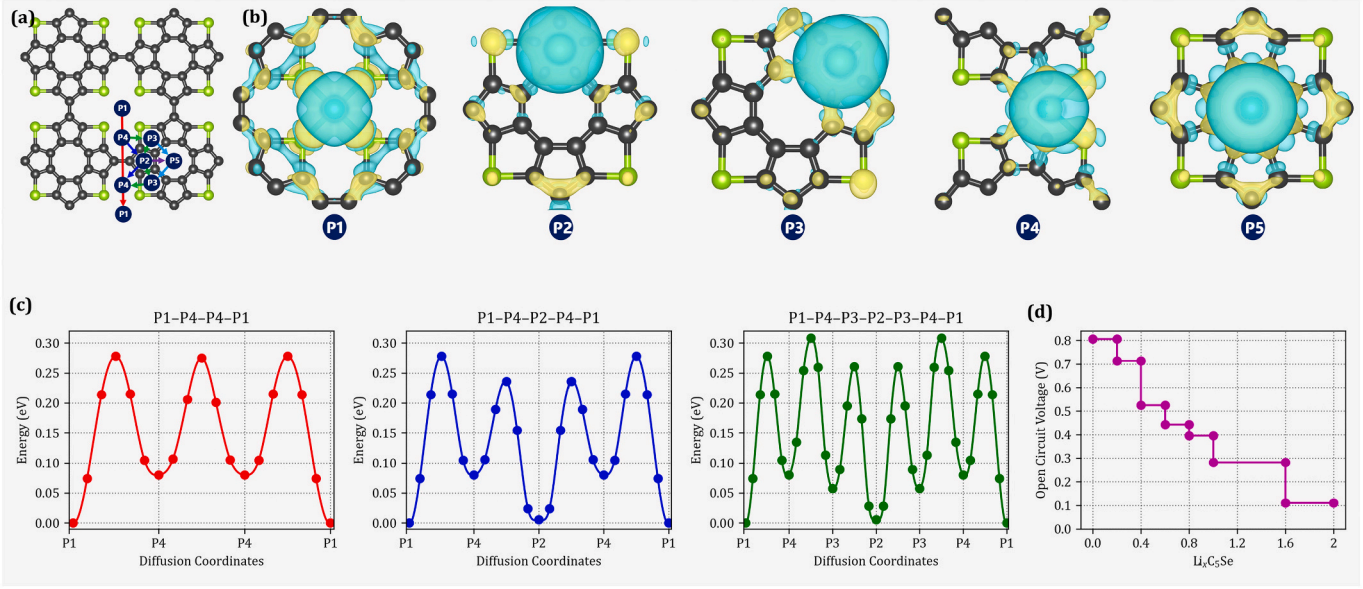

Fig. 10. (a) Different adsorption sites (P1-P5) and possible diffusion pathways of Se-HC monolayer. (b) Differential charge densities of lithiated Se-HC monolayer at different binding sites. (c) Diffusion energy barriers of Li ion on Se-HC monolayer along P1 → P4 → P4 → P1, P1 → P4 → P2 → P4 → P1 and P1 → P4 → P3 → P2 → P3 → P4 → P1. (d) Computed open circuit voltage profile of Se-HC monolayer.

atoms to the Se-HC monolayer at all binding sites. Specifically, 0.89 e-, 0.90 e-, 0.90 e-, 0.90 e-, and 0.91 e- are transferred from the lithium atom to the adsorbate at the P1 through P5 sites, respectively. Differential charge density plots for the Li adsorption sites further demonstrate that charge depletion (cyan coloured region) occurs around the lithium atom, while charge accumulation (yellow coloured region) is observed on the surrounding atoms of the Se-HC monolayer (see Fig. 10b). These findings suggest that lithium undergoes ionization upon adsorption, a critical characteristic that mitigates the formation of lithium clusters and dendrites, thereby enhancing the stability of the Se-HC monolayer during cycling. The diffusion of lithium ions during the charge-discharge process is another crucial factor in determining the performance of a Li-ion battery anode. To assess this, we calculated the diffusion energy barriers for lithium ions moving between the most stable adsorption sites using the climbing-image nudged elastic band (CI-NEB) method, as proposed by Henkelman and co-workers. Different possible diffusion path between the most favourable binding sites are presented in Fig. 10a. Our results show that lithium ions diffuse with minimal barriers between adsorption sites, suggesting efficient ion transport. For instance, when migrating between two P1 sites, the lithium ion follows the path P1 → P4 → P4 → P1 with an effective diffusion barrier of only 0.278 eV, the path P1 → P4 → P2 → P4 → P1 with 0.278 eV and P1 → P4 → P3 → P2 → P3 → P4 → P1 with 0.308 eV as presented in Fig. 10c. This low diffusion barrier indicates that the Se-HC monolayer supports rapid lithium-ion diffusion, which is critical for achieving high-rate battery performance.

Subsequently, we investigated the effect of lithium concentration on the adsorption behaviour of the Se-HC monolayer by incrementally adding lithium atoms to the structure. The average adsorption energy exhibited a decreasing trend as lithium concentration increased, turning positive when the lithium concentration reached beyond 8 atoms. This suggests that the Se-HC monolayer can stably accommodate up to 8 lithium atoms, beyond which lithium clustering may occur. Thus, the Se-HC monolayer can accommodate a maximum of 8 lithium atoms, yielding a molecular formula of $Li_8C_{20}Se_4$.

Further, we calculated the open circuit voltage (OCV) at varying lithium concentrations using the energies of the most favourable intermediate states. The resulting OCV plot, presented in Fig. 10d, reveals a moderate yet stable voltage, consistent with typical Li-ion battery anode behaviour. Finally, we computed the theoretical specific capacity (TSC) using the formula:

$$TSC = xF/M$$

where, x is the concentration of Li atoms and M is the molecular weight of the formula unit (C_5Se) of the Se-HC monolayer and F is the Faraday's constant. Based on this formula, the Se-HC monolayer is predicted to exhibit a theoretical specific capacity of 385.6 mA h g^{-1}. Taken together, these results demonstrate that the Se-HC monolayer offers optimal adsorption energies, low diffusion barriers for fast ion movement, a moderate open circuit voltage, and a significant theoretical storage capacity. These findings highlight the Se-HC monolayer as a promising candidate for Li-ion battery anode applications, offering both high efficiency and stability for next-generation energy storage devices.

Further, we conducted a detailed analysis on comparing the electronic properties and performance characteristics of Se-HC monolayer with several other 2D materials, particularly carbon allotropes, which are often considered for lithium-ion battery anode material applications. As shown in Table 1, Se-HC stands out with a moderate capacity of 386 mAh/g and an attractive diffusion barrier in the range of 0.28–0.31 eV, which is considerably lower than many metallic and semimetallic materials. This allows for improved ion mobility, which is critical for high-performance battery applications. Additionally, the Se-HC monolayer

Table 1
Theoretical storage capacity, diffusion barrier, open circuit voltage (OCV) and electronic properties of different 2D materials.

S. no	2D material	Capacity (mAh/g)	Diffusion barrier (eV)	OCV (V)	Electronic property
1	Se-HC	386	0.28–0.31	0.47	Gapped Dirac material
2	M-graphene	279	0.39	0.03	Metal [71]
3	Graphite	372	0.40	0.11	Metal [72]
4	ψ-Graphene	372	0.31	–	Metal [73]
5	Net-C18	403	0.32	0.02	Metal [74]
6	DOTT	446	0.20–0.90	0.28	Metal [75]
7	TPO12	558	0.60–0.69	0.47	Metal [76]
8	net-τ	558	0.30	0.04	Metal [77]
9	Tolanene	638	0.61–0.71	0.25	Metal [78]
10	h-PAMS	676	0.35	0.29	Metal [79]

exhibits a unique electronic structure characterized by gapped Dirac states, distinguishing it from many metallic materials. Obviously, these properties give Se-HC a distinct advantage for energy storage and battery performance.

5. Conclusions

This study uses state-of-the-art density functional theory calculations to investigate a novel 2D form of Se-based hetero-circulene (Se-HC), typically a carbon-selenide monolayer. Results indicate that the Se-HC monolayer is energetically more favourable than a wide range of 2D carbon selenides, including α-CSe, β-CSe, h-CSe, C_4Se, C_5Se, and C_6Se. Phonon mode analysis, combined with ab initio molecular dynamics simulations, confirms its dynamical and thermal stability, while elastic stress tensor analysis establishes its mechanical stability. Electronic structure calculations reveal that the Se-HC monolayer exhibits gapped Dirac states and massive flat bands, the remarkable features typically observed in monolayer and magic-angle twisted bilayer graphene. Additionally, Se-HC demonstrates strong optical absorption in the near-infrared (NIR) and visible regions, underscoring its potential for infrared photodetection and optoelectronic applications. Furthermore, Se-HC nanoribbons and nanotubes exhibit width- and chirality-dependent electronic properties. Also, the anodic performance of Se-HC monolayer for Li-ion battery applications is particularly promising, featuring optimal adsorption energies, low diffusion energy barriers, and a moderate theoretical storage capacity. These findings highlight Se-HC as a compelling candidate for next-generation quantum materials, photonic devices, and energy applications.

CRediT authorship contribution statement

Naga Venkateswara Rao Nulakani: Writing – review & editing, Writing – original draft, Visualization, Validation, Resources, Methodology, Investigation, Formal analysis, Data curation, Conceptualization. **Yarjan Abdul Samad:** Writing – review & editing, Writing – original draft, Visualization, Conceptualization. **Ameen Shahid:** Writing – review & editing, Writing – original draft. **Calvyn Howells:** Writing – review & editing, Writing – original draft. **Dalaver Hussain Anjum:** Writing – review & editing, Writing – original draft, Visualization, Validation, Supervision, Software, Resources, Project administration, Methodology, Investigation, Funding acquisition, Formal analysis, Data curation, Conceptualization.

Declaration of competing interest

The authors declare that they have no known competing financial interests or personal relationships that could have appeared to influence the work reported in this paper.

Data availability

Data will be made available on request.

Acknowledgements

NVRN and DHA acknowledge the joint KU-UAEU collaboration for financial support under the grant number KU-UAEU-2023-012 and the high-performance computing facility (Almesbar), Khalifa University of Science and Technology, Abu Dhabi, UAE. DHA acknowledges financial support from Khalifa University of Science and Technology, Abu Dhabi, UAE, under the Research and Innovation Grant (RIG-2024-002).

Appendix A. Supplementary data

Supplementary data to this article can be found online at https://doi.org/10.1016/j.est.2025.119110.

References

[1] A.K. Geim, K.S. Novoselov, The rise of graphene, Nat. Mater. 6 (2007) 183–191, https://doi.org/10.1038/nmat1849.
[2] P. Avouris, C. Dimitrakopoulos, Graphene: synthesis and applications, Mater. Today 15 (2012) 86–97, https://doi.org/10.1016/S1369-7021(12)70044-5.
[3] Y. Huang, J. Liang, Y. Chen, An overview of the applications of graphene-based materials in supercapacitors, Small 8 (2012) 1805, https://doi.org/10.1002/smll.201102635.
[4] K.M.F. Shahil, A.A. Balandin, Thermal properties of graphene and multilayer graphene: applications in thermal interface materials, Solid State Commun. 152 (2012) 1331–1340, https://doi.org/10.1016/j.ssc.2012.04.034.
[5] T. Low, P. Avouris, Graphene plasmonics for terahertz to mid-infrared applications, ACS Nano 8 (2014) 1086–1101, https://doi.org/10.1021/nn406627u.
[6] K.S. Novoselov, S.V. Morozov, T.M.G. Mohinddin, L.A. Ponomarenko, D.C. Elias, R. Yang, I.I. Barbolina, P. Blake, T.J. Booth, D. Jiang, J. Giesbers, E.W. Hill, A. K. Geim, Electronic properties of graphene, Phys. Status Solidi B 244 (2007) 4106–4111, https://doi.org/10.1002/pssb.200776208.
[7] A.H.C. Neto, F. Guinea, N.M.R. Peres, K.S. Novoselov, A.K. Geim, The electronic properties of graphene, Rev. Mod. Phys. 81 (2009) 109–162.
[8] K.S. Novoselov, A.K. Geim, S.V. Morozov, D. Jiang, M.I. Katsnelson, I. V. Grigorieva, S.V. Dubonos, A.A. Firsov, Two-dimensional gas of massless Dirac fermions in graphene, Nature 438 (2005) 197–200, https://doi.org/10.1038/nature04233.
[9] A.F. Young, P. Kim, Quantum interference and Klein tunnelling in graphene heterojunctions, Nat. Phys. 5 (2009) 222, https://doi.org/10.1038/nphys1198.
[10] M.I. Katsnelson, K.S. Novoselov, A.K. Geim, Chiral tunnelling and the Klein paradox in graphene, Nat. Phys. 2 (2006) 620–625, https://doi.org/10.1038/nphys384.
[11] X. Du, I. Skachko, A. Barker, E.Y. Andrei, Approaching ballistic transport in suspended graphene, Nat. Nanotechnol. 3 (2008) 491–495, https://doi.org/10.1038/nnano.2008.199.
[12] Y. Zhang, Y.-W. Tan, H.L. Stormer, P. Kim, Experimental observation of the quantum Hall effect and Berry's phase in graphene, Nature 438 (2005) 201–204, https://doi.org/10.1038/nature04235.
[13] N.V.R. Nulakani, V. Subramanian, Computational realization of Dirac nodal point and Dirac nodal loop fermions in novel β-graphyne analogues, J. Mater. Chem. C 6 (2018) 7626–7634, https://doi.org/10.1039/C8TC02386G.
[14] N.V.R. Nulakani, T.J. Dhilip Kumar, Electronic level modelling of graphene-borophene lateral heterostructures as anodes in Li-ion batteries, Appl. Surf. Sci. 614 (2023) 156227, https://doi.org/10.1016/j.apsusc.2022.156227.
[15] N.V.R. Nulakani, M. Kamaraj, V. Subramanian, Coro-graphene and circumcoro-graphyne: novel two-dimensional materials with exciting electronic properties, RSC Adv. 5 (2015) 78910–78916, https://doi.org/10.1039/C5RA14477A.
[16] N.V.R. Nulakani, M.A. Ali, V. Subramanian, A novel quasi-planar two-dimensional carbon sulfide with negative Poisson's ratio and Dirac fermions, ChemPhysChem 24 (2023) e202300266, https://doi.org/10.1002/cphc.202300266.
[17] Z. Wang, X.-F. Zhou, X. Zhang, Q. Zhu, H. Dong, M. Zhao, A.R. Oganov, Phagraphene: a low-energy graphene allotrope composed of 5-6-7 carbon rings with distorted Dirac cones, Nano Lett. 15 (2015) 6182–6186, https://doi.org/10.1021/acs.nanolett.5b02512.
[18] H. Chen, S. Zhang, W. Jiang, C. Zhang, H. Guo, Z. Liu, Z. Wang, F. Liu, X. Niu, Prediction of two-dimensional nodal-line semimetals in a carbon nitride covalent network, J. Mater. Chem. A 6 (2018) 11252–11259, https://doi.org/10.1039/C8TA02555J.
[19] H. Zhang, Y. Li, J. Hou, A. Du, Z. Chen, Dirac state in the FeB_2 monolayer with graphene-like boron sheet, Nano Lett. 16 (2016) 6124–6129, https://doi.org/10.1021/acs.nanolett.6b02335.
[20] L.Z. Zhang, Z.F. Wang, S.X. Du, H. Gao, F. Liu, Prediction of a Dirac state in monolayer TiB_2, Phys. Rev. B 90 (2014) 161402, https://doi.org/10.1103/PhysRevB.90.161402.
[21] F. Schwierz, Graphene transistors: status, prospects, and problems, Proc. IEEE 101 (2013) 1567–1584, https://doi.org/10.1109/JPROC.2013.2257633.
[22] F. Xia, D.B. Farmer, Y. Lin, P. Avouris, Graphene field-effect transistors with high on/off current ratio and large transport band gap at room temperature, Nano Lett. 10 (2010) 715–718, https://doi.org/10.1021/nl9039636.
[23] S. Maharubin, X. Zhang, F. Zhu, H.-C. Zhang, G. Zhang, Y. Zhang, Synthesis and applications of semiconducting graphene, J. Nanomater. 2016 (2016) 1–19, https://doi.org/10.1155/2016/6375962.
[24] G. Lu, K. Yu, Z. Wen, J. Chen, Semiconducting graphene: converting graphene from semimetal to semiconductor, Nanoscale 5 (2013) 1353, https://doi.org/10.1039/c2nr32453a.
[25] J. Nilsson, A.H. Castro Neto, F. Guinea, N.M.R. Peres, Electronic properties of bilayer and multilayer graphene, Phys. Rev. B 78 (2008) 045405, https://doi.org/10.1103/PhysRevB.78.045405.
[26] K. Toko, H. Murata, Layer exchange synthesis of multilayer graphene, Nanotechnology 32 (2021) 472005, https://doi.org/10.1088/1361-6528/ac1d05.
[27] M. Yankowitz, S. Chen, H. Polshyn, Y. Zhang, K. Watanabe, T. Taniguchi, D. Graf, A.F. Young, C.R. Dean, Tuning superconductivity in twisted bilayer graphene, Science 363 (1979) (2019) 1059–1064, https://doi.org/10.1126/science.aav1910.
[28] Y. Zhang, T.-T. Tang, C. Girit, Z. Hao, M.C. Martin, A. Zettl, M.F. Crommie, Y. R. Shen, F. Wang, Direct observation of a widely tunable bandgap in bilayer graphene, Nature 459 (2009) 820–823, https://doi.org/10.1038/nature08105.
[29] T. Ohta, A. Bostwick, T. Seyller, K. Horn, E. Rotenberg, Controlling the electronic structure of bilayer graphene, Science (1979) 313 (2006) 951–954, https://doi.org/10.1126/science.1130681.

[30] E. McCann, D.S.L. Abergel, V.I. Fal'ko, Electrons in bilayer graphene, Solid State Commun. 143 (2007) 110–115, https://doi.org/10.1016/j.ssc.2007.03.054.
[31] E.Y. Andrei, A.H. MacDonald, Graphene bilayers with a twist, Nat. Mater. 19 (2020) 1265–1275, https://doi.org/10.1038/s41563-020-00840-0.
[32] R. Bistritzer, A.H. MacDonald, Moiré bands in twisted double-layer graphene, Proc. Natl. Acad. Sci. 108 (2011) 12233–12237, https://doi.org/10.1073/pnas.1108174108.
[33] Y. Cao, V. Fatemi, A. Demir, S. Fang, S.L. Tomarken, J.Y. Luo, J.D. Sanchez-Yamagishi, K. Watanabe, T. Taniguchi, E. Kaxiras, R.C. Ashoori, P. Jarillo-Herrero, Correlated insulator behaviour at half-filling in magic-angle graphene superlattices, Nature 556 (2018) 80–84, https://doi.org/10.1038/nature26154.
[34] Y. Cao, V. Fatemi, S. Fang, K. Watanabe, T. Taniguchi, E. Kaxiras, P. Jarillo-Herrero, Unconventional superconductivity in magic-angle graphene superlattices, Nature 556 (2018) 43–50, https://doi.org/10.1038/nature26160.
[35] X. Lu, P. Stepanov, W. Yang, M. Xie, M.A. Aamir, I. Das, C. Urgell, K. Watanabe, T. Taniguchi, G. Zhang, A. Bachtold, A.H. MacDonald, D.K. Efetov, Superconductors, orbital magnets and correlated states in magic-angle bilayer graphene, Nature 574 (2019) 653–657, https://doi.org/10.1038/s41586-019-1695-0.
[36] A.L. Sharpe, E.J. Fox, A.W. Barnard, J. Finney, K. Watanabe, T. Taniguchi, M. A. Kastner, D. Goldhaber-Gordon, Emergent ferromagnetism near three-quarters filling in twisted bilayer graphene, Science (1979) 365 (2019) 605–608, https://doi.org/10.1126/science.aaw3780.
[37] Y. Cao, D. Chowdhury, D. Rodan-Legrain, O. Rubies-Bigorda, K. Watanabe, T. Taniguchi, T. Senthil, P. Jarillo-Herrero, Strange metal in magic-angle graphene with near Planckian dissipation, Phys. Rev. Lett. 124 (2020) 076801, https://doi.org/10.1103/PhysRevLett.124.076801.
[38] H.T. Li, T.Z. Ji, R.G. Yan, W.L. Fan, Z.X. Zhang, L. Sun, B.F. Miao, G. Chen, X. G. Wan, H.F. Ding, General method to construct flat bands in two-dimensional lattices, Phys. Rev. Lett. 134 (2025) 076402, https://doi.org/10.1103/PhysRevLett.134.076402.
[39] H. Zhang, Z. Shi, Z. Jiang, M. Yang, J. Zhang, Z. Meng, T. Hu, F. Liu, L. Cheng, Y. Xie, J. Zhuang, H. Feng, W. Hao, D. Shen, Y. Du, Topological flat bands in 2D breathing-Kagome lattice Nb_3 $TeCl_7$, Adv. Mater. 35 (2023) 2301790, https://doi.org/10.1002/adma.202301790.
[40] A. Bhattacharya, I. Timokhin, R. Chatterjee, Q. Yang, A. Mishchenko, Deep learning approach to genome of two-dimensional materials with flat electronic bands, npj Comput. Mater. 9 (2023) 101, https://doi.org/10.1038/s41524-023-01056-x.
[41] X. Huang, X. Han, Y. Dai, X. Xu, J. Yan, M. Huang, P. Ding, D. Zhang, H. Chen, V. Laxmi, X. Wu, L. Liu, Y. Wang, Y. Xu, Y. Huang, Recent progress on fabrication and flat-band physics in 2D transition metal dichalcogenides moiré superlattices, J. Semicond. 44 (2023) 011901, https://doi.org/10.1088/1674-4926/44/1/011901.
[42] Y. Miyake, H. Shinokubo, Hetero[8]circulenes: synthetic progress and intrinsic properties, Chem. Commun. 56 (2020) 15605–15614, https://doi.org/10.1039/D0CC06495E.
[43] G.V. Baryshnikov, B.F. Minaev, N.N. Karaush, V.A. Minaeva, Design of nanoscaled materials based on tetraoxa[8]circulene, Phys. Chem. Chem. Phys. 16 (2014) 6555, https://doi.org/10.1039/c3cp55154g.
[44] J. Yu, Q. Sun, Y. Kawazoe, P. Jena, Stability and properties of 2D porous nanosheets based on tetraoxa[8]circulene analogues, Nanoscale 6 (2014) 14962–14970, https://doi.org/10.1039/C4NR05037A.
[45] A.V. Kuklin, G.V. Baryshnikov, B.F. Minaev, N. Ignatova, H. Ågren, Strong topological states and high charge carrier mobility in tetraoxa[8]circulene nanosheets, J. Phys. Chem. C 122 (2018) 22216–22222, https://doi.org/10.1021/acs.jpcc.8b08596.
[46] L.V. Begunovich, A.V. Kuklin, G.V. Baryshnikov, R.R. Valiev, H. Ågren, Single-layer polymeric tetraoxa[8]circulene modified by s-block metals: toward stable spin qubits and novel superconductors, Nanoscale 13 (2021) 4799–4811, https://doi.org/10.1039/D0NR08554E.
[47] N.G. Petrov, P. Chartier, T. Maris, J.D. Wuest, Designing tetraoxa[8]circulenes to serve as hosts and sensors, J. Am. Chem. Soc. 144 (2022) 556–572, https://doi.org/10.1021/jacs.1c11728.
[48] P.W. Fritz, T. Chen, T. Ashirov, A. Nguyen, M. Dincă, A. Coskun, Fully conjugated tetraoxa[8]circulene-based porous semiconducting polymers, Angew. Chem. Int. Ed. 61 (2022) e202116527, https://doi.org/10.1002/anie.202116527.
[49] P.W. Fritz, T. Ashirov, A. Coskun, Porous organic polymers with heterocyclic crown ethers for selective lithium-ion capture, Chem 10 (2024) 2207–2219, https://doi.org/10.1016/j.chempr.2024.03.014.
[50] G. Li, W. Guo, Q. Hou, Z. Liu, X. Li, Y. Yong, Improvement of gas-sensing performance of TO8C monolayers as high-efficient room-temperature NO and NO_2 gas sensors induced by electric field, Results Phys. 61 (2024) 107770, https://doi.org/10.1016/j.rinp.2024.107770.
[51] E.V. Anikina, D.V. Babailova, M.S. Zhilin, V.P. Beskachko, Tetraoxa[8]circulene monolayer as hydrogen storage material: model with Boys–Bernardi corrections within density functional theory, J. Surf. Invest. 18 (2024) 19–26, https://doi.org/10.1134/S102745102401004X.
[52] G. Kresse, J. Furthmüller, Efficient iterative schemes for *ab initio* total-energy calculations using a plane-wave basis set, Phys. Rev. B 54 (1996) 11169–11186, https://doi.org/10.1103/PhysRevB.54.11169.
[53] G. Kresse, J. Furthmüller, Efficiency of ab-initio total energy calculations for metals and semiconductors using a plane-wave basis set, Comput. Mater. Sci. 6 (1996) 15–50, https://doi.org/10.1016/0927-0256(96)00008-0.
[54] P.E. Blöchl, Projector augmented-wave method, Phys. Rev. B 50 (1994) 17953–17979, https://doi.org/10.1103/PhysRevB.50.17953.
[55] J.P. Perdew, K. Burke, M. Ernzerhof, Generalized gradient approximation made simple, Phys. Rev. Lett. 77 (1996) 3865–3868, https://doi.org/10.1103/PhysRevLett.77.3865.
[56] H.J. Monkhorst, J.D. Pack, Special points for Brillouin-zone integrations, Phys. Rev. B 13 (1976) 5188–5192, https://doi.org/10.1103/PhysRevB.13.5188.
[57] S. Grimme, J. Antony, S. Ehrlich, H. Krieg, A consistent and accurate *ab initio* parametrization of density functional dispersion correction (DFT-D) for the 94 elements H-Pu, J. Chem. Phys. 132 (2010) 154104, https://doi.org/10.1063/1.3382344.
[58] S. Grimme, Semiempirical GGA-type density functional constructed with a long-range dispersion correction, J. Comput. Chem. 27 (2006) 1787–1799, https://doi.org/10.1002/jcc.20495.
[59] Q. Zhang, T. Xin, X. Lu, Y. Wang, Optoelectronic properties of X-doped (X = O, S, Te) photovoltaic CSe with puckered structure, Materials 11 (2018) 431, https://doi.org/10.3390/ma11030431.
[60] Q. Zhang, Y. Feng, X. Chen, W. Zhang, L. Wu, Y. Wang, Designing a novel monolayer β-CSe for high performance photovoltaic device: an isoelectronic counterpart of blue phosphorene, Nanomaterials 9 (2019) 598, https://doi.org/10.3390/nano9040598.
[61] X. Zhou, L. Qian, H. Huang, Z. Yuan, Y. Hu, Hydrogenated h-CSe as a promising 2D direct semiconductor for optoelectronic applications, Phys. B Condens. Matter 691 (2024) 416179, https://doi.org/10.1016/j.physb.2024.416179.
[62] N.V.R. Nulakani, V. Subramanian, A theoretical study on the design, structure, and electronic properties of novel forms of graphynes, J. Phys. Chem. C 120 (2016) 15153–15161, https://doi.org/10.1021/acs.jpcc.6b03562.
[63] P. Kong, X. Zhang, J. Wang, W. Tian, Y. Ni, B. Sun, H. Wang, H. Wang, Y.P. Feng, Y. Chen, Electron-phonon coupling superconductivity and tunable topological state in carbon-rich selenide monolayers, Phys. Rev. B 107 (2023) 184115, https://doi.org/10.1103/PhysRevB.107.184115.
[64] J. Guan, Z. Zhu, D. Tománek, Phase coexistence and metal-insulator transition in few-layer phosphorene: a computational study, Phys. Rev. Lett. 113 (2014) 046804, https://doi.org/10.1103/PhysRevLett.113.046804.
[65] Q. Lu, J. Cook, X. Zhang, K.Y. Chen, M. Snyder, D.T. Nguyen, P.V.S. Reddy, B. Qin, S. Zhan, L.-D. Zhao, P.J. Kowalczyk, S.A. Brown, T.-C. Chiang, S.A. Yang, T.-R. Chang, G. Bian, Realization of unpinned two-dimensional Dirac states in antimony atomic layers, Nat. Commun. 13 (2022) 4603, https://doi.org/10.1038/s41467-022-32327-8.
[66] E.H. Hasdeo, L.P.A. Krisna, M.Y. Hanna, B.E. Gunara, N.T. Hung, A.R.T. Nugraha, Optimal band gap for improved thermoelectric performance of two-dimensional Dirac materials, J. Appl. Phys. 126 (2019) 035109, https://doi.org/10.1063/1.5100985.
[67] Z. Chen, Y. Hu, Z. Zhu, W. Zhang, Tunable Dirac cones in single-layer selenium, New J. Phys. 22 (2020) 093055, https://doi.org/10.1088/1367-2630/abb43b.
[68] S. Huang, M. Sanderson, J. Tian, Q. Chen, F. Wang, C. Zhang, Hot carrier relaxation in three dimensional gapped Dirac semi-metals, J. Phys. D. Appl. Phys. 51 (2018) 015101, https://doi.org/10.1088/1361-6463/aa994b.
[69] V.Yu. Tsaran, S.G. Sharapov, Landau levels and magnetic oscillations in gapped Dirac materials with intrinsic Rashba interaction, Phys. Rev. B 90 (2014) 205417, https://doi.org/10.1103/PhysRevB.90.205417.
[70] H. Bandi, R. Dahule, A.K. Kakarla, R. Maezono, D. Narsimulu, S.W. Akram, R. Shanthappa, J.S. Yu, Green synthesis and interface engineering of $CoMoO_4$–Ag heterostructures: enhanced electrochemical performance for lithium-ion batteries, Chem. Eng. J. 508 (2025) 160748, https://doi.org/10.1016/j.cej.2025.160748.
[71] C. Kou, Y. Tian, M. Zhang, E. Zurek, X. Qu, X. Wang, K. Yin, Y. Yan, L. Gao, M. Lu, W. Yang, M-graphene: a metastable two-dimensional carbon allotrope, 2D Mater. 7 (2020) 025047, https://doi.org/10.1088/2053-1583/ab7977.
[72] K. Persson, Y. Hinuma, Y.S. Meng, A. Van der Ven, G. Ceder, Thermodynamic and kinetic properties of the Li-graphite system from first-principles calculations, Phys. Rev. B 82 (2010) 125416, https://doi.org/10.1103/PhysRevB.82.125416.
[73] X. Li, Q. Wang, P. Jena, ψ-Graphene: a new metallic allotrope of planar carbon with potential applications as anode materials for lithium-ion batteries, J. Phys. Chem. Lett. 8 (2017) 3234–3241, https://doi.org/10.1021/acs.jpclett.7b01364.
[74] X.H. Cai, Q. Yang, S. Zheng, M. Wang, Net-C18: a predicted two-dimensional planar carbon allotrope and potential for an anode in lithium-ion battery, Energy Environ. Mater. 4 (2021) 458–464, https://doi.org/10.1002/eem2.12127.
[75] K.A.L. Lima, A.V.P. Abreu, A.M.A. Silva, L.A. Ribeiro, First-principles and machine learning insights into the design of DOTT-carbon and its lithium-ion storage capacity, J. Mater. Chem. A 13 (2025) 15609–15619, https://doi.org/10.1039/D5TA01619C.
[76] D. Bhattacharya, D. Jana, TPO12-graphene: a new two-dimensional metallic carbon with 4–5 ring for Lithium ion battery, Appl. Surf. Sci. 669 (2024) 160495, https://doi.org/10.1016/j.apsusc.2024.160495.
[77] X. Wang, Z. Feng, J. Rong, Y. Zhang, Y. Zhong, J. Feng, X. Yu, Z. Zhan, Planar net-τ: a new high-performance metallic carbon anode material for lithium-ion batteries, Carbon 142 (2019) 438–444, https://doi.org/10.1016/j.carbon.2018.10.075.
[78] S. Ullah, M.G. Menezes, A.M. Silva, Theoretical characterization of tolanene: a new 2D sp-sp^2 hybridized carbon allotrope, Carbon 217 (2024) 118618, https://doi.org/10.1016/j.carbon.2023.118618.
[79] T. Zeng, H. Yang, H. Wang, G. Chen, Acepentalene membrane sheet: a metallic two-dimensional carbon allotrope with high carrier mobility for lithium ion battery anodes, J. Phys. Chem. C 124 (2020) 5999–6011, https://doi.org/10.1021/acs.jpcc.0c00376.